Soil Dynamics and Earthquake Engineering 184 (2024) 108726

Contents lists available at ScienceDirect

Soil Dynamics and Earthquake Engineering

journal homepage: www.elsevier.com/locate/soildyn

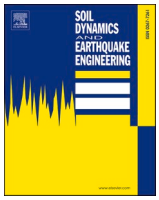

Application of the material point method (MPM) to characterise the impact forces of granular landslides on rigid obstacles

M. Kontoe *, S. Lopez-Querol, T. Rossetto

Department of Civil, Environmental and Geomatic Engineering, U.C.L., London, UK

ARTICLE INFO

Keywords:
MPM
Dry granular flows
Soil impact force
Rigid structures
Flume experiment
Scaling laws

ABSTRACT

This study deploys the Material Point Method (MPM) to investigate the soil pressures exerted on a 3D rigid obstacle partially obstructing a dry granular flow; a configuration not previously addressed in the literature on a numerical modelling basis. A 2D simulation is first developed and validated against a flume experiment that monitors the interaction of dry granular flows with retaining structures under varying flume angles. The model is then extended to 3D, enabling the adjustment of the obstacle's geometry to observe the impact of granular flows on impermeable rigid obstacles partially obstructing the soil material. The trend in the recorded soil forces exhibits an initial peak that occurs simultaneously with the first impact, followed by a steep degradation branch as the soil deposits in front of the structure, thus reducing the flow's dynamics. The numerical simulation is subsequently upscaled to ensure that macroscopic dimensional analysis adequately interprets small-scale numerical observations to mimic prototype conditions using the MPM approach. Simplified factors are finally derived to represent the response characteristics of large-scale simulations based on the original findings.

1. Introduction

Recent landslide events, such as the 2017 Mocoa landslide in Colombia and the 2022 Petropolis landslide in Rio De Janeiro, Brazil, have highlighted the severe impact of such hazards on communities and infrastructure. The 2017 Mocoa landslide, triggered by heavy rain, led to a mudflow affecting over 45,000 individuals, including 329 fatalities, and impacting more than 17 neighbourhoods [1]. Similarly, the 2022 Petropolis landslide resulted in a death toll exceeding 230 people and caused nearly 200 million $ of economic losses [2,3]. Nepal experiences annual landslides during the monsoon periods. Only in 2020, 243 fatalities and 51 missing individuals were reported [4]. These are only a few examples of catastrophic landslides taking place every year in the world.

To mitigate the devastating consequences of landslides, a reliable characterisation for soil pressures exerted on buildings and infrastructure is essential. This can be investigated through large-scale experiments [5] and field observations (e.g., [6–8]). However, these approaches involve significant costs and implementation challenges, thus, it is more common to perform small-scale flume tests (e.g., [9–12]) and adopt large-strain analysis numerical methods for monitoring soil-to-structure interaction (e.g., [13–15]).

Both small-scale experiments and numerical models often simulate landslides in the form of frictional, dry granular flows, typically resulting in a pile-up interaction mechanism with the retaining structures under investigation. As per Fig. 1, this mechanism involves three stages: a static zone (deposit) initially forms after the first impact *(stage 1)*, partially obstructing the incoming flow and forcing the soil material to ascend over the existing sediment with reduced dynamics *(stage 2)*; the soil progressively accumulates at the front of the obstacle until it reaches a maximum height; the dynamics of the incoming granular flow are insufficient for the soil to climb over the sediment mound resulting in further deposition upstream of it *(stage 3)* [16,17]. The interaction between the static zone and the incoming soil plays a crucial role in dissipating the energy of the flow, protecting the obstacle from experiencing a large impact force. This leads the normal forces acting on the obstacle to show an initial rapid increase to a peak value influenced by the velocity of the incoming flow during stage 1. Subsequently, the force exhibits a gradual reduction to a residual value in stages 2 and 3, respectively, attributed to the decreasing effect of the dynamic impact on the obstacle and increasing contribution of the applied static load from the sediment [18].

Most of the past studies focused on analysing the impact of soil flows on full-width retaining structures. However, limited research is

* Corresponding author.
E-mail address: m.kontoe.17@ucl.ac.uk (M. Kontoe).

https://doi.org/10.1016/j.soildyn.2024.108726
Received 21 September 2023; Received in revised form 7 May 2024; Accepted 16 May 2024
Available online 14 July 2024

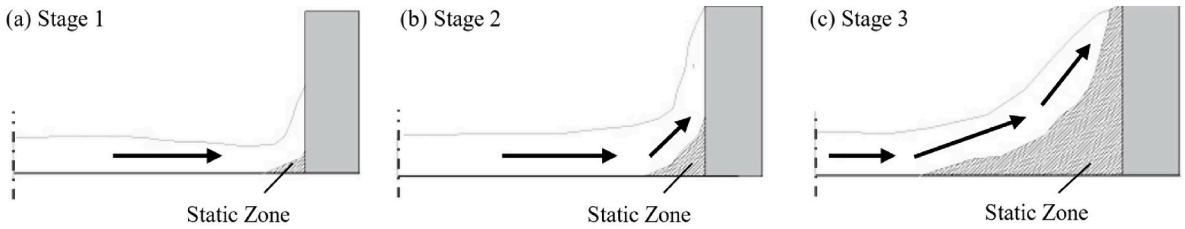

Fig. 1. Interaction mechanism of dry granular flows with retaining structures.

available on the interaction of landslides with obstacles of varying geometries, which are more representative of the different components of built environment. To the authors' knowledge, only one small-scale experimental study by Zanuttigh and Lamberti [19] attempted to quantify the induced soil forces on obstacles that represent buildings and dams. To address this gap, one of the objectives of the current paper is the numerical investigation of the impact mechanism and force pattern exerted on obstacles narrower than the flow section, which can provide useful insight into the fundamental principles associated with this interaction process. This is achieved by developing an advanced numerical model and validating it based on the results of a past flume experiment that assessed the interaction of dry granular flows with a full width retaining structure. This serves as the baseline for analysing the model with different geometric configurations for the obstacle.

It is also acknowledged that the use of small-scale experiments for simulating landslides has several downsides because the actual physical behaviour of soil flows varies across different scales [20]. Therefore, this paper also attempts to address this limitation by upscaling the geometry of the modelled flume experiment using multiple scaling ratios to represent different prototype conditions. Simplified factors are then derived for modifying the landslide response parameters (e.g., flow velocity, impact forces) when obtained through numerical modelling, based on the adopted geometric scaling ratio. This derivation relies on the similarity of Froude number observed across the different geometric scales of the developed numerical models, which is an essential assumption in macroscopic dimensional analysis (e.g., [10,21]) to ensure that the experimental response mimics the real dynamic, kinematic, and geometric conditions.

This paper is organised as follows: Section 2 outlines the general methodology including the adopted numerical method and the case-study experiment; Section 3 describes the validation of the numerical model of the flume test on the experimental findings; Section 4 addresses numerically the interaction of soil flows with obstacles partially obstructing the incoming granular material. It also presents the effect of numerically scaling the laboratory setup on the performance of the soil flow; Section 5 summarises the main conclusions derived from this study.

2. Methodology

This study investigates the effect of partially obstructing a dry granular flow on the impact mechanism using the Material Point Method (MPM) as a modelling strategy. The adopted methodology is outlined in Fig. 2. Initially, a simulation of the flume experiment performed by Moriguchi et al. [18] is developed. The experiment investigated the interaction of dry granular flows with a full-width retaining obstacle and served as means of validation of the employed numerical assumptions. Specifically, a sensitivity analysis is conducted on the mesh size and the number of material points representing the granular flow to ensure consistency between the numerical results and the experimental findings.

The geometry of the simulated obstacle is subsequently modified, by gradually reducing the width of the structure, to examine the influence of different blockage ratios (i.e. ratio of obstacle width to flume width) on the soil flow-structure interaction process. The numerically obtained normal forces at the front of the obstacle are qualitatively compared with the experimental observations of Zanuttigh & Lamberti [19]. The flexibility of the numerical model allows for simulating additional configurations, through adjusting the inclination of the flume and the height of the obstacle. MPM analysis contributes to monitoring aspects of this problem that have not been previously documented, including the interaction mechanism, the impact flow velocity, the progressive formation of the stagnant zone around the obstacle, and the exerted shear forces on the sides of the structure.

Since the developed models refer to laboratory setups, the original simulation is geometrically upscaled, by 10 and 20 times, to reflect prototype conditions and investigate the subsequent performance of the numerical model across different scales. The numerical findings lead to the proposal of suitable formulations for transforming key parameters of the original simulation to represent the upscaled configurations. The derived scaling principles are assessed against the formulations proposed by Iai et al. [22], which were developed upon fundamental physical laws and validated against experimental findings. This comparison provides insights into the reliability of the derived factors and contributes to comprehending the ability of MPM to capture scale effects.

2.1. Material point method (MPM)

The Material Point Method (MPM, [23]) is a mesh-based numerical method combining the Eulerian and Lagrangian principles to model large deformation problems and capture the coupled hydromechanical response of soils. The computational domain is discretised into a fixed Eulerian background mesh and the continuum is represented by a set of Lagrangian points. Fig. 3 illustrates the solution scheme of this numerical method performed during each analysis step [24]. The required information, stored in the particles, is mapped through linear shape functions to the nodes (Figs. 3–1) to solve the governing equations of motion (Figs. 3–2). The obtained variables are then, transferred to the material points (Fig. 3–3) and the mesh returns to its original state while discarding the relevant information to the numerical solution (Figs. 3–4).

The formulations integrated within this computational framework allow large-strain analysis, since numerical instabilities associated with the excessive distortion of the mesh are not present [24]. In addition, the ability of MPM to simulate and address the interaction between the constituent phases of the medium contributes to capturing the evolution of excess water pressure, which could potentially induce slope instability [25]. Therefore, this approach is deemed appropriate to investigate the failure mechanisms of collapsing slopes triggered either by precipitation or ground shaking. Previous studies deploy this numerical technique to capture the response of recorded landslide events [26–28] and of small-scale experiments on miniaturised slopes and soil flows (e.g., [26,29–31]).

This study adopts the MPM formulations as integrated within the open-source software Anura3D (www.anura3d.com). The implemented dynamic solution algorithm incorporates an explicit integration scheme which requires a small-time increment, automatically estimated by the software, to ensure the stability of the numerical results. For linear systems, Fern et al. [25] propose a critical time step (Δt_{cr}) equal to the

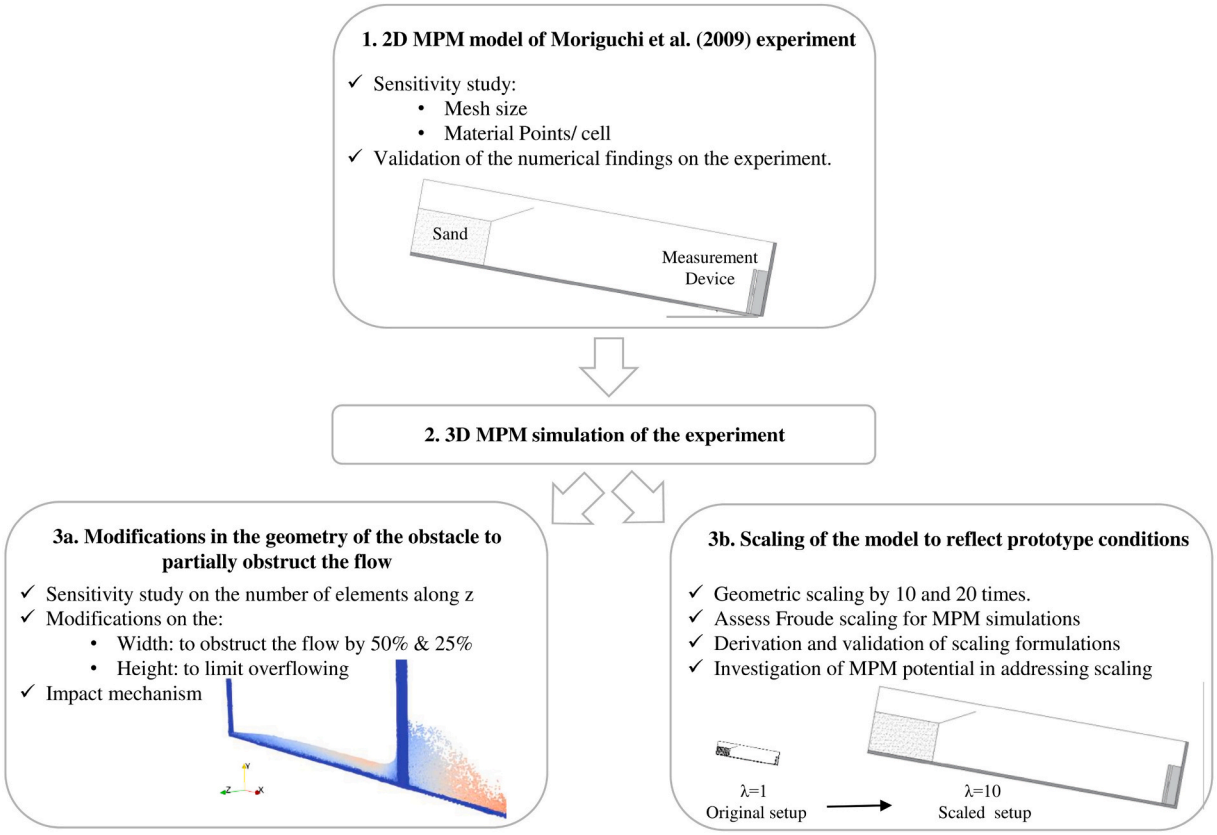

Fig. 2. Outline of the methodology.

duration required by a wave of speed c, to cross the smallest element of dimension d. In non-linear systems, Δt_{cr} should be further adjusted by the Courant number, C_{NB} ($0 < C_{NB} < 1$). The stability of the numerical solution is also considerably influenced by the deployed low-order shape functions. MPM uses linear shape functions to increase the computational efficiency of the analysis which leads to the cell-crossing and kinematic locking instabilities. Cell-crossing, initially reported by Zhou et al. [32], consists of induced oscillations (noise) to the obtained solution. Anura3D provides the option of combining the Gauss and the MPM integration methods for evaluating the stresses over the mesh elements located inside and at the boundaries of the medium, respectively [33]. This method has been deployed from past studies in the literature to limit the effect of the present instability [29,34]. Kinematic locking is another significant issue encountered in MPM. It is observed through the numerically predicted erroneous field stresses and unrealistic velocities for the material points, as highlighted by Mast et al. [35]. Among the existing methodologies in the literature, the current software deploys the Nodal Mixed Discretisation approach (NDM) [36], which according to Al-Kafaji [34] adequately addresses the locking effect.

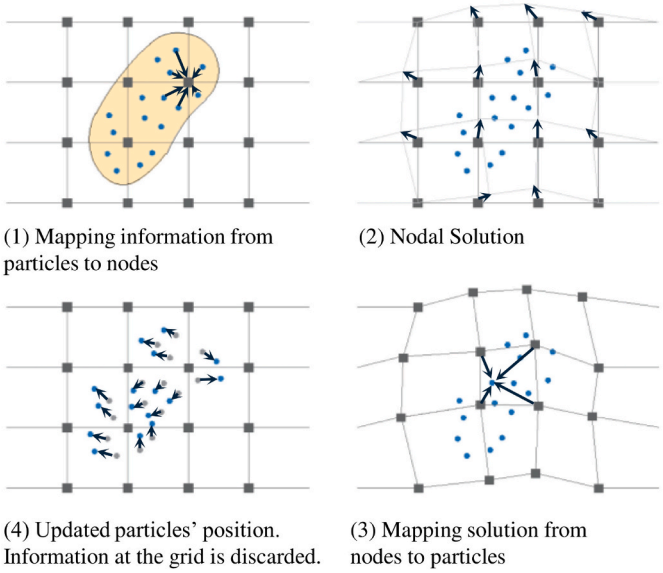

Fig. 3. MPM computational cycle, after Soga et al.[24].

2.1.1. Contact behaviour

To simulate the interaction of individual bodies and evaluate the nodal forces along their contact interface, Anura3D incorporates the Bardenhagen et al. [37] algorithm. This approach effectively accounts for both sliding and adhesion at the contact surface, while it also improves the accuracy of the predicted velocities for the individual bodies to align with the system's kinematics, as specified by the contact law [38].

Initially, the software calculates the nodal accelerations for the each of the bodies, as well as for the combined system, to obtain the nodal velocities in the subsequent time step. The analysis investigates whether the bodies tend to separate or approach each other at the nodes of a predefined contact surface, while considering the velocity components perpendicular to the contact node. The normal and tangential forces of a body g, at an approaching node k are evaluated in line with Equations (1) and (2), respectively.

$$f_{norm}^{t+\Delta t} = \frac{m_{k,g}^{t}}{\Delta t} v_{norm}^{t+\Delta t} \tag{1}$$

$$f_{tan}^{t+\Delta t} = \frac{m_{k,g}^{t}}{\Delta t} v_{tan}^{t+\Delta t} \tag{2}$$

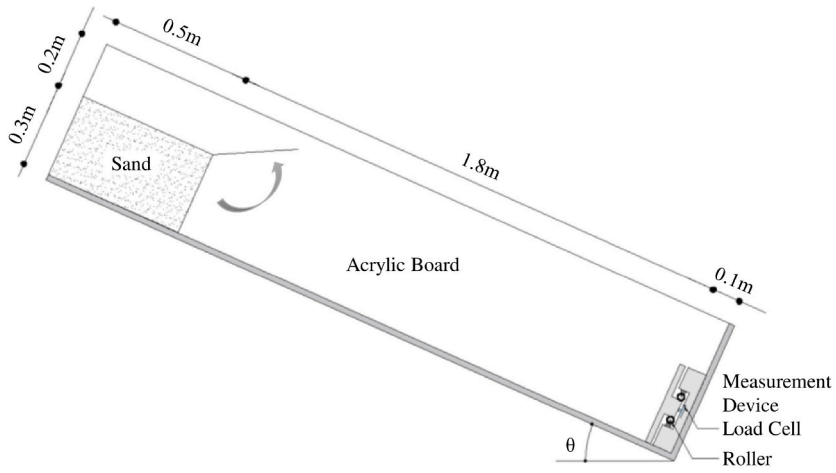

Fig. 4. Geometry of flume experiment, after Moriguchi et al. [18].

where, v_{norm} , v_{tan} denote the normal and tangential velocity components, f_{norm}, f_{tan} refer to the normal and tangential force components, $m_{k,g}$ represents the nodal mass integrated from the material points of body g.

On the condition that the individual bodies approach each other, the algorithm examines their potential for sticking or sliding. If sliding occurs, the algorithm aligns the normal velocity of each body with that of the system to prevent inter-penetration. This adjustment influences the normal force component, in Equation (1). Due to sliding, the magnitude of the tangential force, governed by Equation (4), is determined based on the updated normal force. Adhesion is calculated using Equation (3). The adjustments introduced to Equation (4) leads to also applying a correction to the tangential velocity. These modifications ensure a more accurate representation of the system's response during sliding conditions.

$$f_{adh} = \alpha A_k^t \tag{3}$$

$$f_{tan}{}^{t+\Delta t} = \left(f_{adh}{}^{t+\Delta t} + \mu \left| f_{norm}{}^{t+\Delta t} \right|\right)\boldsymbol{t} \tag{4}$$

where, f_{adh} represents the adhesive force, α is the adhesion, A_k^t denotes the contact area of node k, μ corresponds to the friction coefficient, $\boldsymbol{t}$ refers to the unit vector in the direction of the tangent.

Subsequently, the acceleration at the contact nodes for each of the bodies is re-evaluated and deployed to re-assess the velocity of the MPs, respectively. This process is performed for both bodies in direct contact. To determine the reaction force along the contact interface, Anura3D integrates the reaction forces across the nodes of the predefined contact plane of the bodies/materials.

2.2. Description of the case study experiment

The numerical models of this study simulate the experimental response of the small-scale flume tests performed by Moriguchi et al. [18]. The experiments investigated the impact of the flume's inclination on the measured normal forces at the front of a rigid obstacle, owing to the interaction with a dry granular flow. Fig. 4 illustrates the setup of the flume experiment, with inclination angles of 45, 50, 55, 60, and 65° being tested.

A box filled with dry Toyoura sand, of 50kg weight was placed at the top of the flume. The door of the box opened promptly to allow the granular material to flow towards the 0.3m height rigid box, located at the end of the flume. This structure, representing a full-width obstacle, qualifies as a measurement device consisting of a front impact surface, two rollers and a load cell attached to a stiff base. The soil force, acting on the front element, is smoothly transmitted to the recording instrument with the contribution of the provided rollers. The flume base was coated with granular material to ensure friction between the soil flow and the apparatus. The interface between the soil and the side acrylic boards was perceived as smooth. Five experimental trials were conducted for each flume configuration and considerable increase was observed in the magnitude of the recorded peak impact forces with increasing flume angles.

3. Numerical model of the flume test

3.1. 2D simulation

A 2D simulation of the test is initially developed to validate the selected numerical modelling strategy against experimental response. This constitutes a starting point towards extending the model into 3D at a later stage for investigating the soil pressures on rigid obstacles with geometries different from retaining structures. This simulation adopts the numerical assumptions suggested by Cuomo et al. [14], where a 2D MPM model was calibrated with the same experiments as herein and provided results compliant with the measurements of the laboratory tests.

Despite the inclined configuration of the experimental setup, the flume is here modelled as being horizontal. To account for the influence of the tested angles on the interaction of the granular flow with the rigid obstacle, the gravity components are adjusted such that they act perpendicular to the flume long axis. The downstream boundaries of the computational domain are extended to accommodate the potential overflow of the granular material beyond the obstacle. The Mohr-Coulomb constitutive law is employed to describe the response of the granular material, while the obstacle and the boundaries of the apparatus are modelled as elastic elements. The assigned properties of the material models are summarised in Table 1 and they are consistent with the values prescribed by Cuomo et al. [14]. To attain similar behaviour with the validated reference model from the literature, identical contact properties are deployed to characterise the interaction of the soil flow with the components of the experimental apparatus. Therefore, a frictional contact angle of 40° is assigned along the base of the flume, while the interface between the soil and the obstacle is considered smooth.

The prescribed boundary conditions of the 2D computational domain are presented in Fig. 5. To limit the movement of the material points beyond the boundaries of the model, the top and lateral sides of the computational domain are restrained in the vertical (u_y) and horizontal (u_x) directions respectively, while the base is modelled as fixed ($u_{x,y}$). To initialise the stresses of the numerical model to reflect the gravity conditions of the experimental setup, the flume is first subjected to static analysis. During this step, the soil mass remains undeformed by

Table 1
Material properties after Cuomo et al. [14].

Material	Density ρ_s *(kg/m^3)*	Porosity n	Elastic Modulus E *(MPa)*	Cohesion c *(kPa)*	Friction angle φ *(°)*	Dilatancy angle ψ *(°)*
Dry sand	2650	0.48	20	0	40	0
Obstacle	7850	0	Rigid	–	–	–
Flume	7850	0	Rigid	–	–	–

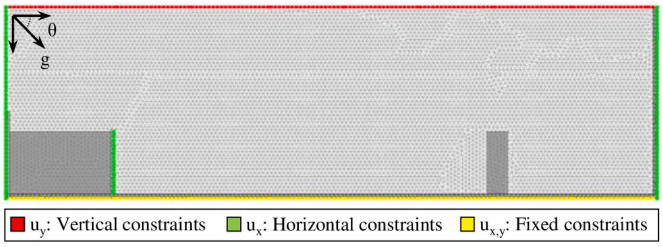

Fig. 5. Constraints to the computational domain during the stress initialisation process.

restraining the lateral movement (u_x) of the integration points in the box, as illustrated in Fig. 5. Subsequently, these additional fixities are removed to allow the propagation of the granular material and capture the dynamic response of the soil flow. The rest of the boundary conditions remain identical in both static and dynamic analyses to ensure that the displaced MPs are limited within the computational domain. The sequential dynamic analysis is divided into 20 load-steps with a time increment of 0.1sec to reproduce the recorded duration of the experiments, i.e. 2sec. Consistently with the recommendations by Fern et al. [25], a local damping factor of 0.75 is applied for the static analysis to facilitate the convergence of the numerical solution, while for the dynamic analysis, a value of 0.05 is employed to account for the inherent damping of the soil. To address the common numerical instabilities associated with the implementation of typical MPM, the mixed integration scheme and the strain smoothening technique (NDM), available in Anura3D, are adopted.

The MPM simulations developed in this study are analysed adopting identical flume angles to the ones tested in the original experiment. The soil impact forces at the front of the obstacle are directly calculated by the software via integrating the nodal reactions estimated over the face of the element. The force measurements are post-processed in MATLAB to reduce oscillations, remove the outliers and obtain the mean-trendline of the data. The data exceeding three median absolute deviations from the local median are identified as outliers and are ignored in the fitting process. Finally, the trend of the data is derived by fitting a Gaussian curve to appropriately represent the recorded response.

3.1.1. *Sensitivity analysis of modelling parameters*

To achieve the stability of the numerical solution, an initial parametric study is conducted on the size of the background mesh and the required number of integration points provided per cell. The original background mesh with triangular elements of 0.02m size, depicted in Fig. 5, is progressively densified at the front of the obstacle. The findings from the sensitivity analysis conducted on the simulation of the experimental setup with a flume angle of 65°, when considering element sizes of 0.02m, 0.01m and 0.0085m, are presented in Fig. 6. To achieve comparable measurements with the experiment, the total normal impact force recorded by Anura3D at the front of the obstacle is multiplied by the width of the structure in the laboratory setup, i.e. 0.3m. To address the mean trend of the numerical results, a Gaussian curve is fitted to the raw data. The study reveals that decreasing the mesh size, while maintaining a constant number of MPs across the models, i.e. 4955 MPs, leads to a reduction in the peak impact force measurements. Specifically, the peak value decreases from 800N to 730N and further to 590N for mesh sizes of 0.02m, 0.01m, and 0.0085m, respectively. Refinement of the mesh is seen to enhance the accuracy of the numerical solution and improve the range of the recorded oscillations, particularly during the initial impact. It is worth noting that the MPM results shown in the following figure have not been post-processed to remove outliers. The significantly oscillating forces in Fig. 6, manifest the presence of volumetric locking, as discussed by Wang et al. [39]. This instability arises from using low-order shape functions coupled with employing a large number of MPs, aimed at limiting the presence of empty cells during the analysis [29,40], which leads to over-stiffening the response of the model. However, reducing the mesh size leads to partially limiting the effect of volumetric locking, as evidenced by the results of the sensitivity analysis on mesh size.

Assuming that the dimension of the element at the front of the

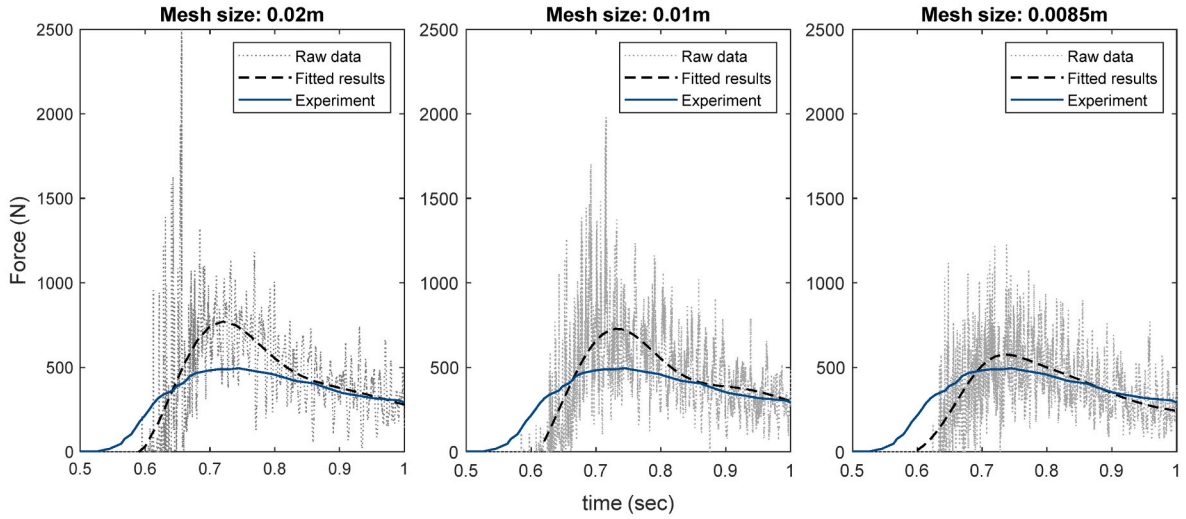

Fig. 6. Impact of the element size on the numerical data.

Table 2
Sensitivity analysis on the number of material points.

MPs/cell of the soil box	Total number of MPs for the granular flow	Peak Impact Force (N)
1	825	465
3	2477	530
6	4955	574
16	13261	570

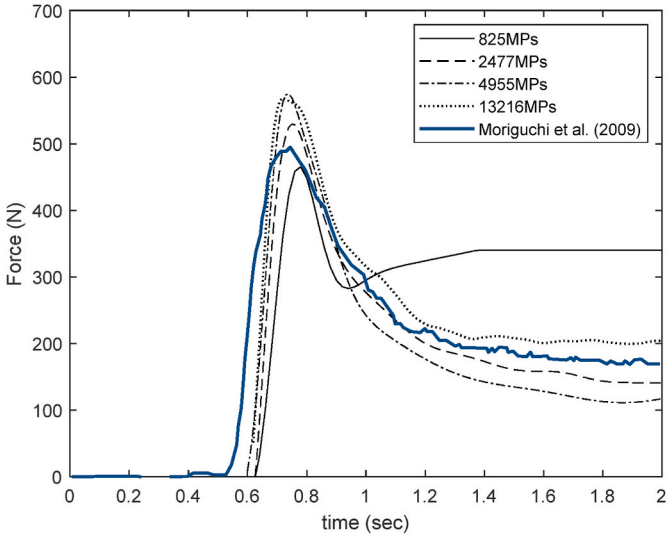

Fig. 7. Sensitivity study on the number of MPs/cell for mesh size equal to 0.0085 m

obstacle is 0.0085 m, in line with the results of the conducted sensitivity analysis on the mesh size, the number of MPs/cell in the soil box is varied. Specifically, 1, 3, 6 and 16 MPs are provided per cell of the soil box, corresponding to 825, 2477, 4955 and 13261 total integration points representing the granular flow as presented in Table 2. The boundaries of the flume apparatus, as well as the rigid obstacle, are represented by 1 MP/cell since the integration points are not expected to move among adjacent elements.

The numerical findings, illustrated in Fig. 7, indicate that for a given mesh size, the numerical solution converges for more than 6MPs/cell of the soil box. The force trendlines remain consistent in terms of the recorded magnitude of impact loads, nearly equal to 570N, as shown in Table 2. In line with Fern et al. [25], increasing the MPs beyond the minimum number required to achieve numerical convergence, has a negligible effect on the results. However, it increases the computational demand from 120sec to 240sec per analysis step.

Fig. 7 demonstrates consistent behaviour between the experimental and numerical measurements for the convergent models, suggesting that the simulations adequately characterise the impact process. However, the numerically recorded peak impact, i.e. 570N, exceeds the experimentally measured forces, which range between 470N and 513N across the five repetitions of the experiment. The observed discrepancy is attributed to the deployed material model. Ceccato and Simonini [41] investigated the influence of different material models, including Mohr-Coulomb model, on a MPM simulation of the same experiment. They concluded that the employed constitutive laws are incapable of capturing the energy dissipation present in a dense granular flow. As a result, while the analyses successfully replicated the experimental soil-structure behaviour, they overpredicted the forces.

Fig. 8 provides a comparison between the normal forces obtained at the front surface of the obstacle, multiplied by the width of the experimental retaining structure, i.e. 0.3m, and those presented by Moriguchi et al. [18] (adopting the modelling parameters obtained from the

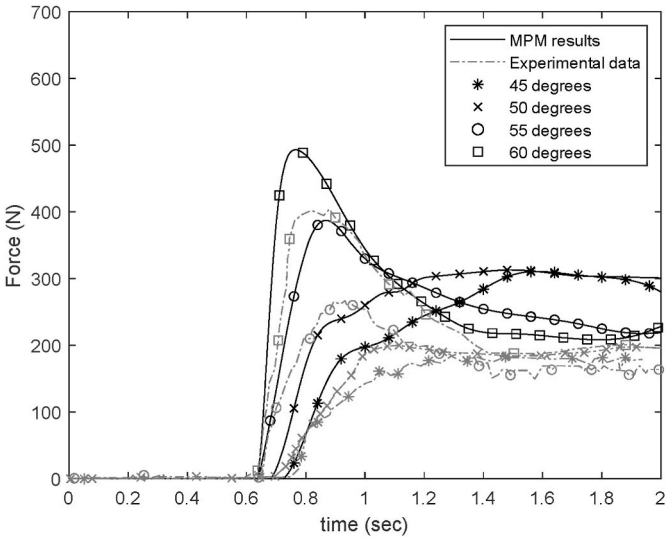

Fig. 8. Comparison of MPM analysis results with Moriguchi et al. [18].

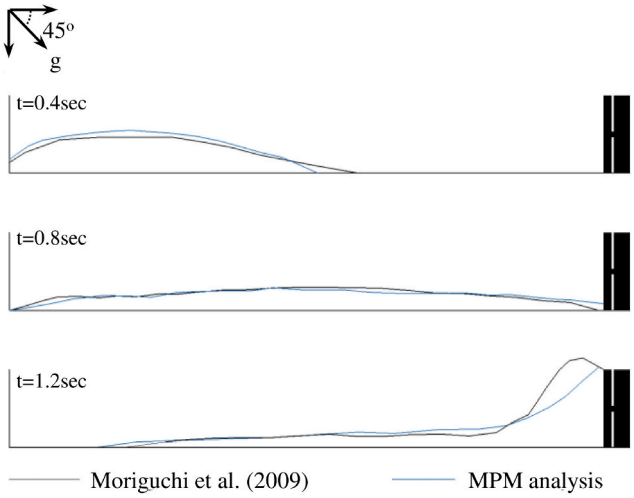

Fig. 9. Deformed shape of granular flow for flume inclination equal to 45°.

performed sensitivity analysis). The observed similarity in the force patterns demonstrates that the present analyses capture impact processes that are consistent with the experiments. Both the numerical and the laboratory findings indicate a steep rise to the peak magnitude as the granular flow first impacts the obstacle, which then gradually decreases towards attaining a residual value. Similarly to the reported response in the experiments, the maximum force as well as, the inclination of the post-peak branch decrease with the flume angle owing to the static pressure being the dominant component in the measured soil pressures. However, the overestimation in the force magnitude linked to the employed material model, as emphasised by Ceccato and Simonini [41], becomes evident in the subsequent analyses. Likewise, these authors numerically obtained peak impact force values of approximately 700N, 490N, 300N and 280N for the 60°, 55°, 50° and 45° flume setups of the same experiment, respectively.

To further test the performance of the numerical model, the deformed shape of the granular flow captured at different time steps, (i.e. 0.4sec, 0.8sec, 1.2sec), is compared with the results of Moriguchi et al. [18] for the 45° flume angle. The qualitative comparison, depicted in Fig. 9, shows that the developed models appropriately represent the experimental response. Unlike in the numerical models, the experimental setup prevents potential overflowing beyond the obstacle. Subsequently, the numerically captured deformed shape of the flow at the

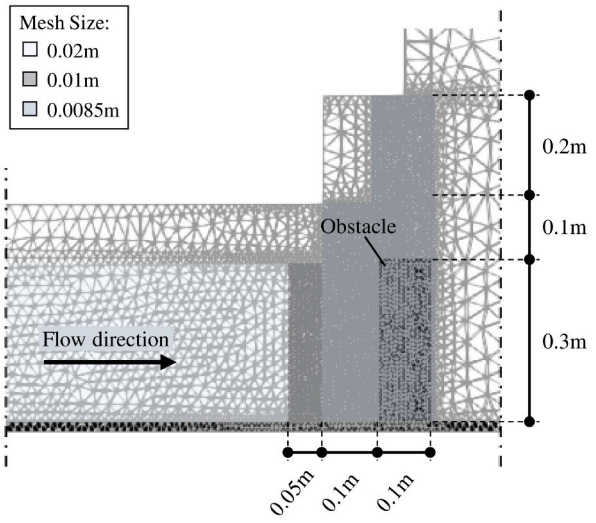

Fig. 10. Detail of the discretised domain in the vicinity of the obstacle.

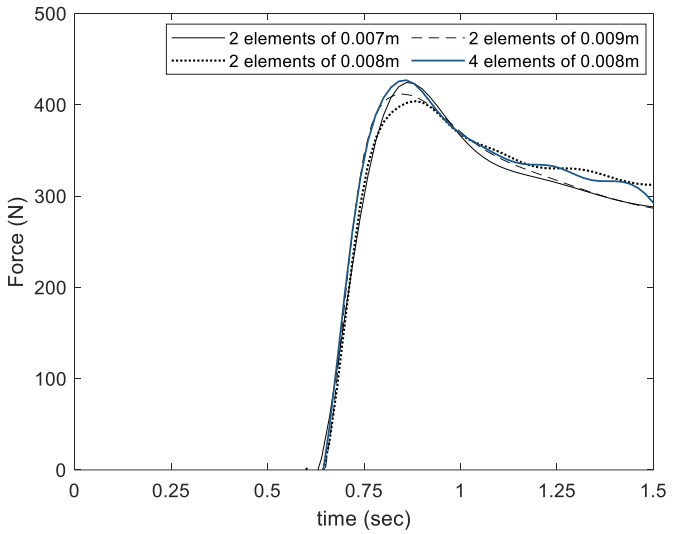

Fig. 11. Sensitivity study on the mesh size and number of elements along z for 55° flume setup.

front of the obstacle differs from the experiment at 1.2sec. It is observed that despite the challenges in accurately predicting the force magnitude, MPM proves to be a suitable algorithm for capturing the evolution of the granular flow. The comparison reveals that the performance of the normal impact forces measured at the front face of the obstacle, along with the deformed shape of the flow captured at different time steps align with the experimental outcomes. In light of these observations, this approach is deemed suitable for investigating the impact of a granular flow on a reduced-width obstacle, to observe variations in the impact process and the profile of recorded forces.

3.2. 3D modelling assumptions

The flume models are extended to the 3D domain, to facilitate modifications in the geometry of the obstacle and investigate numerically the effect of the reduced blockage ratio on the captured impact mechanism and the recorded soil pressures. A parametric study of the 3D model is initially conducted assuming the presence of a full-width retaining structure, to explore the impact of the size and number of elements provided along the width of the flume on the numerical solution. This approach aims to obtain results comparable with the findings of the 2D simulations, ensuring the validity of the adopted modelling strategy. The background mesh in the xy plane of the 3D simulations aligns with the one resulting from the sensitivity study on the 2D model. The discretised domain around the obstacle is illustrated in Fig. 10. Roller supports are provided along the xy planes of the computational domain, to restrict the out-of-plane movement of the material points beyond the limits of the model.

The effect of the number of segments assigned along the z direction of the model is initially tested. Assuming a segment size of 0.008m, two and four elements are provided in the numerical models to ensure consistency in the captured soil pressures among the tested configurations, regardless the dimension of flume. To obtain comparable results, Fig. 11 demonstrates the measurements normalised against the simulated obstacle widths and adjusted to the original dimension of the retaining structure in the experiment, i.e. 0.3m. Given the consistency of the captured force trendlines, the size of the elements along z is further modified, i.e. 0.007m and 0.009m, while assuming two segments, to capture potential variability on the measured impact. The simulation results for the 55° flume experiment are insensitive to both the size and number of elements modelled along z, since the analyses provided identical solutions. The sensitivity study reveals the spatial convergence and stability of the numerical results.

The developed 3D simulations, represent the originally modelled two-dimensional problem, since the support conditions restrict the out of plane movement of the material points. Subsequently, as illustrated in Fig. 12(a), the impact forces measured through the present analyses approximate the corresponding results derived from the 2D models for flume angles of 55 and 45°. As discussed in section 3.1.1, the numerical models tend to overpredict the magnitude of impact forces compared to the experiments. However, the 3D simulations effectively capture both the soil-structure interaction mechanism and the response of the impact forces. It is noted that the deformed shape of the flow in the 3D flume model with an inclination of 45° is consistent with the experimental response, as illustrated in Fig. 12(b), further ensuring the reliability of the implemented modelling strategy.

4. Results

4.1. Partial obstruction of the soil flow

4.1.1. Convergence of the numerical solution

Similarly to the full-width retaining structure configuration, a parametric investigation is conducted to ensure the spatial convergence of numerical results, in the presence of an obstacle causing partial obstruction to the incoming flow. This study explores the effect of altering the number of elements provided along the z axis of the model, while assuming a constant flume width.

The geometry of the original model is adjusted to accommodate a 50% obstruction of the soil flow. Half of the flume apparatus is modelled to reduce the computational demand of the analysis. The obstacle is assumed to be centrally located across the width of the flume, resulting in a symmetric problem. The simulated portion of the flume is divided into two and four segments, along z, of sizes equal to 0.016m and 0.008m accordingly, as shown in Fig. 13. The dashed blue line on this figure illustrates the plane of symmetry for the flume model. Identical contact properties and boundary conditions to the ones prescribed in the original simulation with a full-width obstacle are prescribed in the present analyses. The following results assume a flume angle of 55° degrees.

Fig. 14 presents the normal force, measured at the face of the obstacle for the tested numerical models. The frontal impact is initially normalised by the width of the simulated element (N/m) and then, multiplied by the corresponding dimension of the obstacle in the experiment, i.e. 0.3m, to derive results comparable with those obtained from the original models with full-width retaining structures. The numerical findings indicate a consistent response across all simulations,

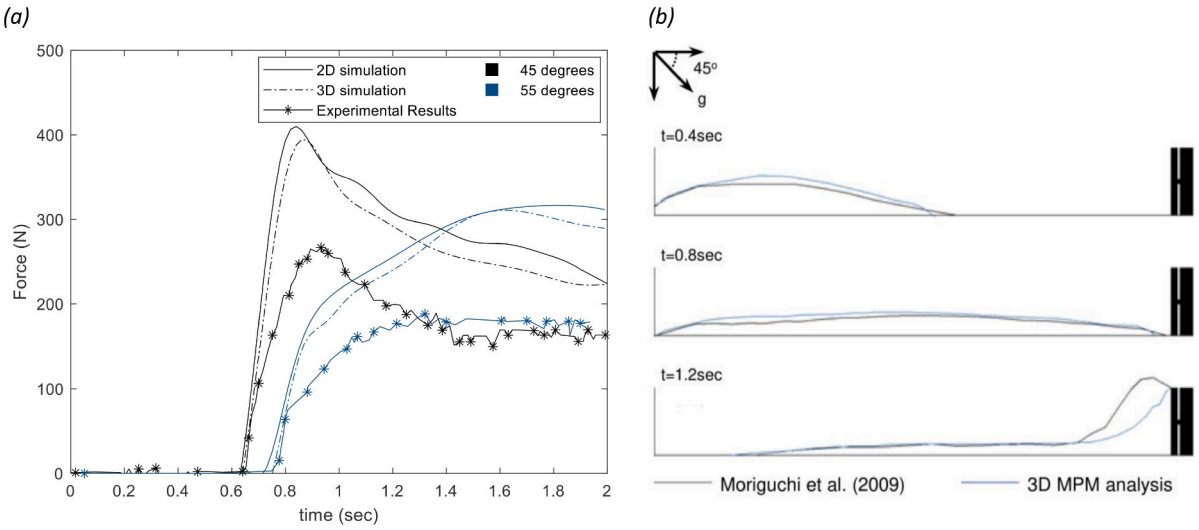

Fig. 12. 3D simulation results comparison (a) of impact forces with the 2D model and the experiment for flume angles of 45° and 55° (b) of the flow response with the experiment for flume angle of 45.°

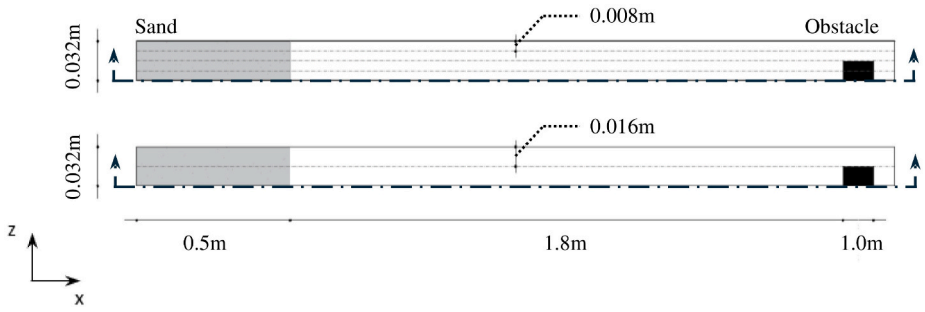

Fig. 13. Plan view of the simulated flume with 4 and 2 segments along z, for 50% obstruction.

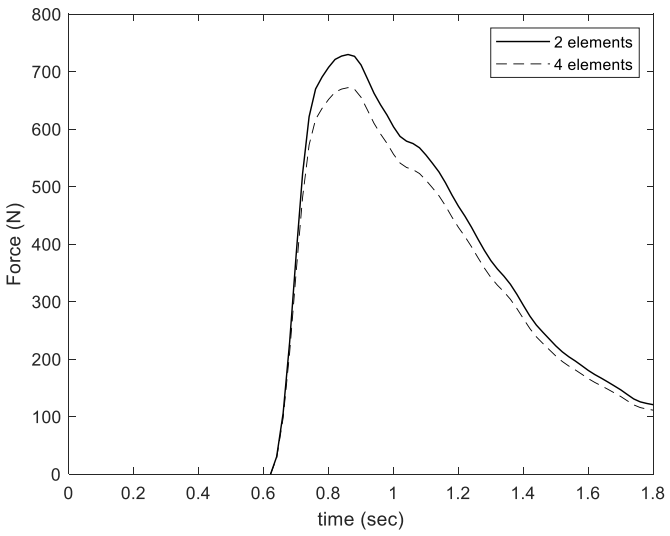

Fig. 14. Normal force measurements from the sensitivity study on models with 50% obstruction.

with a slight decrease in the peak impact force observed in the model using four elements, attributed to the reduced size of the deployed mesh.

Fig. 15 compares the response of the flow, in the vicinity of the obstacle, as captured through the present models, at different sections along the flume width (w), i.e. S1, S2, S3. The captured impact process is identical in both simulations since the deformed shape of the flow exhibits similar performance. However, when comparing section S3 for the two models, it is evident that the simulation with 4 elements along the width of the flume, discharges an increased amount of soil along the section height, attributed to the increased number of material points modelled in this configuration. Despite achieving convergence in the tested models, subsequent analyses adopt four elements across the flume width to capture the flow around the obstacle in enhanced detail. Due to the complexity of the interaction process, the grid was refined to achieve a more precise definition of the flow pattern.

4.1.2. *Impact mechanism*

The geometry of the original simulation is subsequently modified to provide an insight into the soil forces acting on a rigid and impermeable obstacle of reduced width with respect to the dimension of the flume. Four elements of 0.008m are allocated along the section of the flume. The dimension of the obstacle is modified, i.e. 0.016m and 0.008m, to induce a 50% and 25% obstruction of the soil flow, respectively. In addition, to prevent the soil mass from overtopping the structure, the height of the element is increased to 1m. Table 3 summarises the geometric properties of the performed simulations, inducing partial obstruction to the granular flow, along with the corresponding legends deployed in the present section.

The soil impact forces are measured at the front plane and the side of the obstacle to identify the external loads applying to the superstructure. The validation of the numerical model for the full-width retaining structure against the observations from the literature contributes to ensuring that the following analyses represent adequately the impact process.

Fig. 16 demonstrates the normal and shear forces acting on the

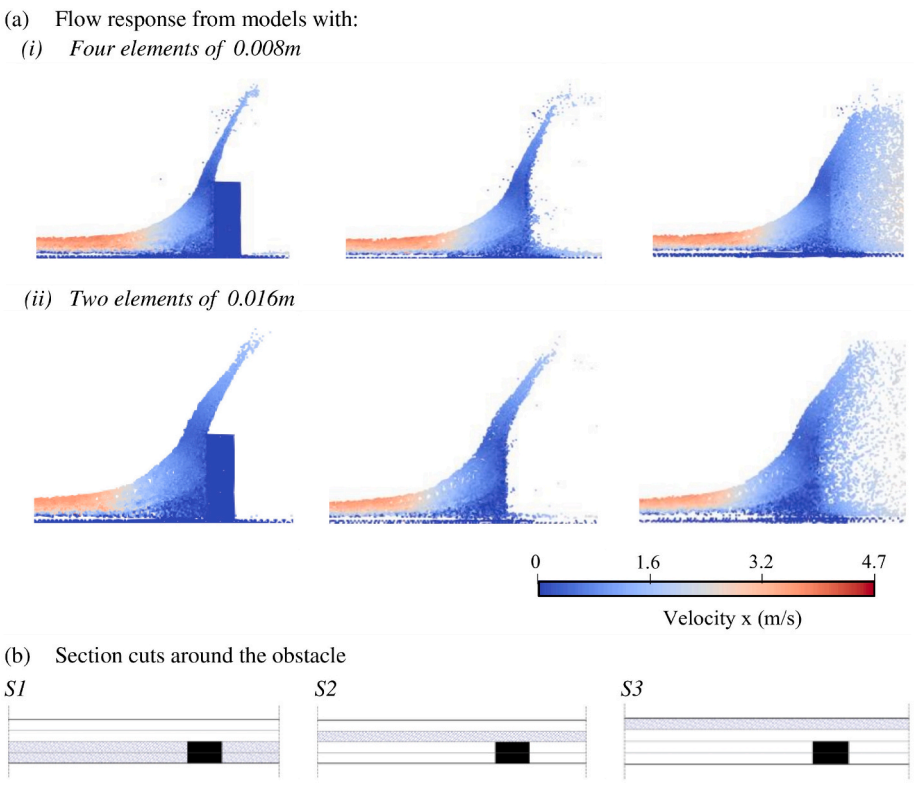

Fig. 15. (a) Impact mechanisms captured from MPM simulations across the (b) sections of the flume.

Table 3
Captions for simulations with partial obstruction (φ refers to the flume angle, i.e. 45° and 55°).

Obstacle height	Blockage ratio	Legend
1) 0.3m	50%	SL φ _0.5
2) 1m	50%	SH φ _0.5
3) 0.3m	25%	SL φ _0.25
4) 1m	25%	SH φ _0.25

simulated geometries of the obstacle, considering a flume inclination of 55°. The shear force curves represent the total load measured at the side of the structure. To correlate the response of the curves with the impact process, assuming the original height of the obstacle, i.e. 0.3m, Fig. 17 provides the evolution of the soil-structure interaction for model SL55_0.5, at key timeframes during the analysis. The illustrated sections are in line with those identified in Fig. 15(b).

The normal force exhibits a steep increase to the peak value following the first impact as demonstrated in Fig. 16. The interaction of the granular flow with the obstacle results in a uniform soil run-up across the entire width of the flume, as shown in Fig. 17a(i). Moreover, a portion of the granular material in contact with the front face of the obstacle diverts towards the corners and discharges through its sides, as per Fig. 17b(i). The diverted soil combines with the incoming material from the segments at the sides of the obstacle and the mass discharges via generating streamlines at the top and bottom of the element, as illustrated in Fig. 17a

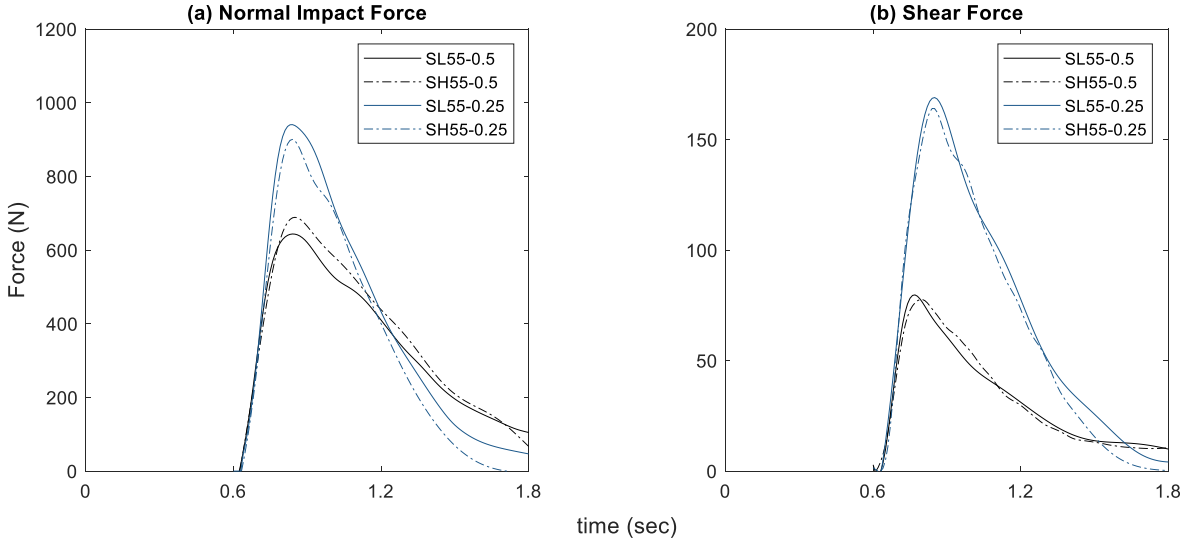

Fig. 16. (a), (b) Impact forces on obstacles inducing partial obstruction to the flow, for 55° flume angle.

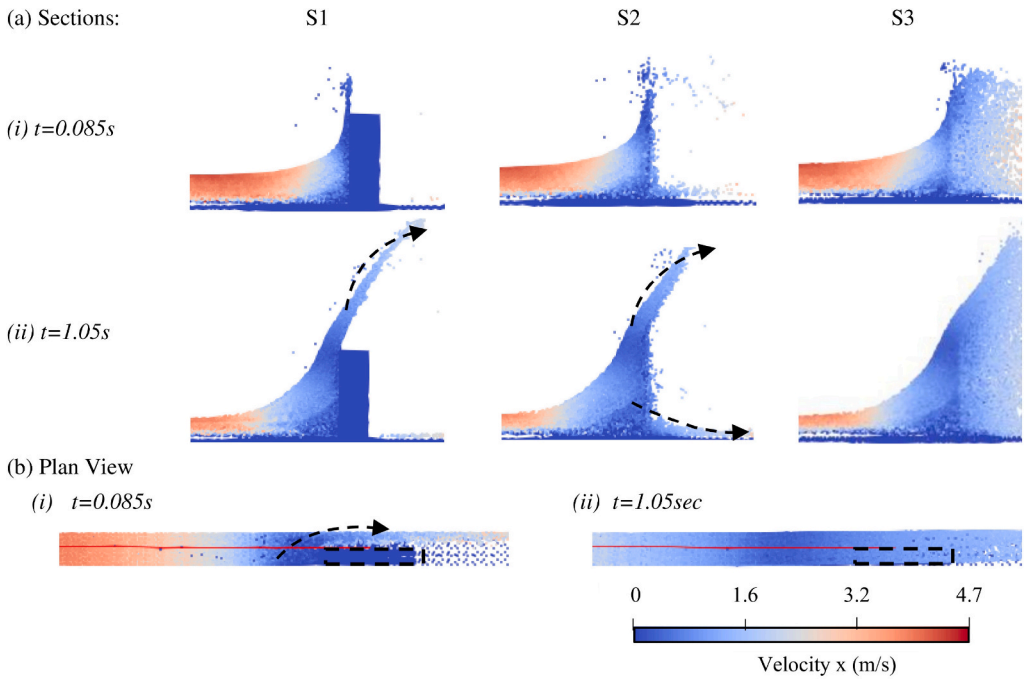

Fig. 17. Evolution of impact process (a) at section-cuts S1, S2 and S3 & (b) in plan.

(ii). By 0.85sec of the analysis, the flow's run-up at the front of the element exceeds the height of the structure and the material overtops the obstacle, providing an additional streamline for soil discharge. Subsequently, the impact force reaches the maximum value, followed by a post-peak degradation branch associated with the continuously reducing dynamics of the incoming flow and the substantial soil discharge. Concurrently, the

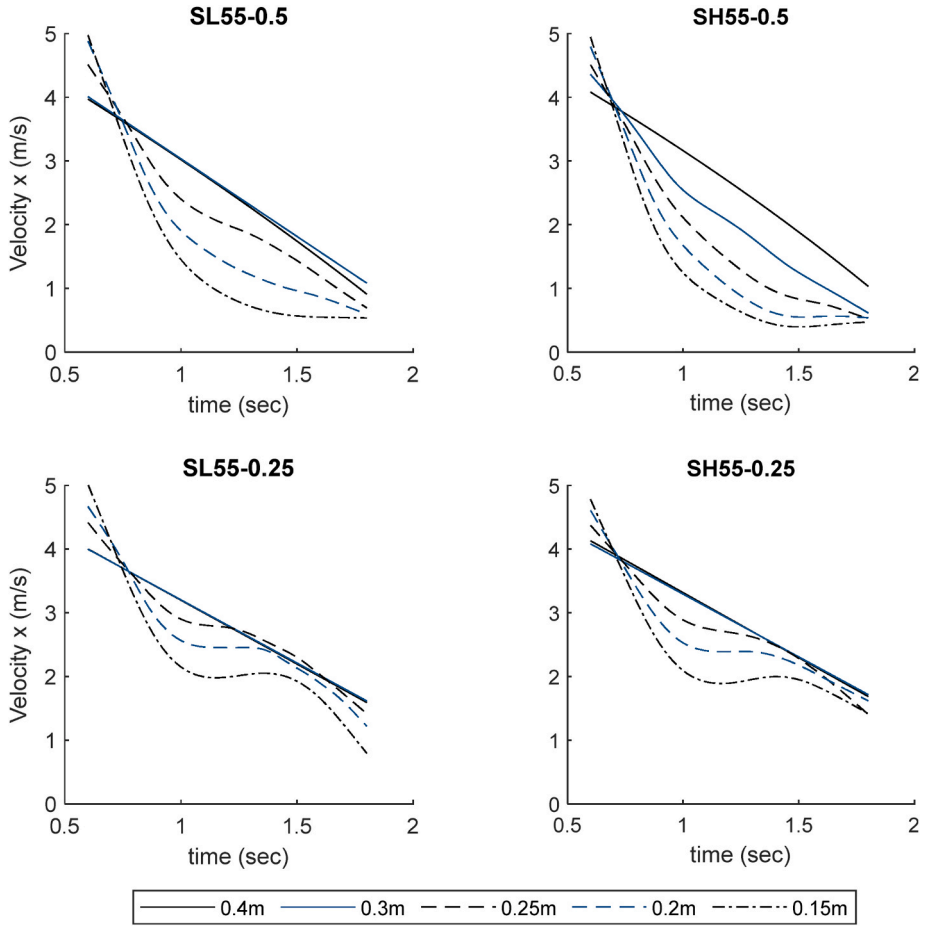

Fig. 18. Average flow velocity measured at different sections upstream of the obstacle for 55° flume angle.

flow height upstream of the obstacle decreases and the material overtopping gradually ceases at 1.85sec. Consistent response to the one described for SL55_0.5 is observed for the simulation with increased obstacle height (SH55_0.5) however, overflowing is obstructed in the latter configuration. The material continuously runs-up across the flume section, reaching a peak height of 0.8m, at almost 0.85sec when the maximum force is recorded. The interaction process described for 50% partial obstruction of the flow is also representative of the impact mechanism observed in simulations with elements obstructing 25% of the incoming flow, i.e. SL55_0.25 & SH55_0.25.

Fig. 16 demonstrates that gradually reducing the width of the obstacle results in an increase in the magnitude of forces acting on the superstructure. Specifically, the peak impact measured from the original simulation with a full-width retaining structure is 400N, while for 50% and 25% obstruction of the flow, the normal force increases to 740N and 940N, respectively. Zanuttigh & Lamberti [19] experimentally investigated the impact of dry granular avalanches on rigid models of houses with different orientations to vary the width of the structure exposed to the incoming flow. These authors also concluded that reducing the obstruction to the flow leads to significantly amplifying the recorded forces.

The first interaction of the incoming flows with the obstacle immediately leads to the formation of stagnant zones. The sediment volume increases over time, altering the flow dynamics near the obstacle. The soil flow velocity, illustrated in Fig. 18, is measured at different sections upstream of the obstacle, i.e. at 0.15m, 0.2m, 0.25m, 0.3m, 0.4m. At 0.4m, the velocity is consistent across all models. The impact of sedimentation, encountered due to the reduction in the flow velocity, is observed approximately 0.25-0.3m upstream of the obstacle for SL55_0.5 and SH55_0.5. The same is observed in the case of SL55_0.25 and SH55_0.25 configurations at nearly 0.15m.

The progressive formation of the static zone, which affects the rate of reduction in flow velocity, depends on the geometry of the obstacle. The evolution of sedimentation process at the front of the obstacle is depicted in Fig. 19. Decreasing the width of the obstacle restricts the extent of the deposit as the soil mass climbs over the existing sediment due to the increased soil flow velocity. The deposit in SL55_0.25 has a steeper slope with respect to that related to SL55_05 and extends only 0.15-0.2m upstream of the obstacle. Subsequently, the runout distance of the incoming flow gradually decreases in the SL55_05 case, imposing a further restriction of the flow dynamics. Nearly identical trends are observed in the sedimentation process of the simulations with obstacles blocking the overflowing mechanism. The current obstacle's geometry results in stagnant zones similar to the original ones, considering the same blockage ratio. As a result, the influence of the deposit on reducing flow dynamics remains consistent across the SL55 and SH55 configurations.

The blockage ratio is a crucial parameter for determining the magnitude of normal forces acting on the obstacle. Specifically, the substantial sediment accumulation in front of obstacles causing 50% partial obstruction to the flow effectively reduces the impact velocity and limits the interaction with the incoming flow. The efficiency of sediments in protecting obstacles from the impact of these flows improves as the obstacle's width increase, leading to smaller normal impact forces.

The shear forces recorded at the sides of the obstacle exhibit an initial peak, coinciding with substantial soil discharge downstream of the element, followed by a subsequent degrading branch. Decreasing the width of the element leads to an increased magnitude of shear forces, attributed to higher velocity of material points passing by the side of the obstacle and enhanced soil mass discharge. It is noted that the sediment remains uniform near the obstacle but gradually decreases along the flume width.

Fig. 20 illustrates the force measurements acquired from simulations with a 45-degree flume angle, showing trends consistent with those observed in the models with a 55-degree flume angle. Specifically, decreasing the obstacle width results in higher peak impact forces and steeper post-peak degradation branches.

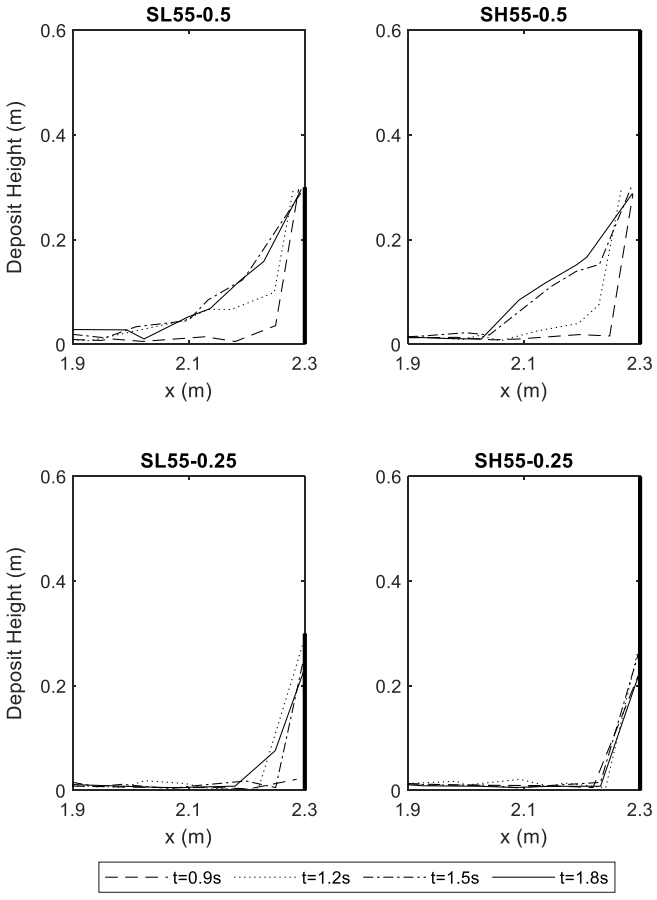

Fig. 19. Static zone at the front of the element.

4.2. Numerical scaling of soil impact forces to prototype conditions

The simulation of the experimental setup with a flume angle equal to 45°, is geometrically upscaled by the factor λ to reflect prototype conditions and investigate numerically the response of the model across different scales. The geometry of the experiment is adjusted by increasing the dimensions of the original model by 10 and 20 times. This implementation aims at establishing analytical formulations to interpret key response variables of the small-scale numerical models into describing upscaled conditions and explore the potential of MPM in addressing scaling effects. Previous experimental studies suggest that the Froude number, *Fr*, is an appropriate dimensional parameter to characterise the dynamic behaviour of soil flows. As a result, attaining Froude similarity across different scales ensures comparable responses among the laboratory tests and field conditions within a macroscopic framework. Since the current application adopts a dry material, the inevitable scale-effects encountered in the presence of interstitial fluids when testing the response of debris-flows is limited [19]. The Froude number distribution achieved through the simulated configurations is evaluated in accordance with Equation (5), prior to the impact of the soil flows on the rigid obstacle.

$$Fr = \frac{v}{\sqrt{gl\cos\alpha}} \tag{5}$$

where, g denotes the gravity acceleration, v is the flow velocity parallel to the base of the flume. The velocity component of the MPs coincides with the horizontal *(x)* global axis of the model since the experiment is

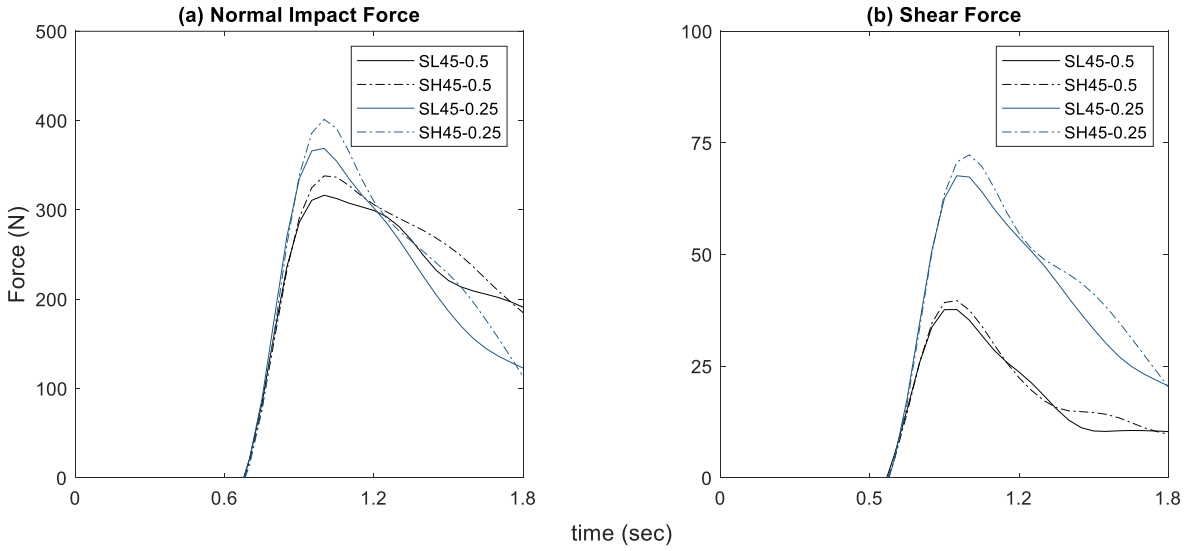

Fig. 20. (a), (b) Impact forces on obstacles inducing partial obstruction to the flow, for 45° flume angle.

modelled horizontally; l is the clear depth of the flow from the base of the flume. The vertical distance of the MPs from the base $(y_{MP}\text{-}y_b)$ aligns with the vertical (y) global axis of the model; α is the flume angle to project the gravity vector on the vertical global axis of the model.

Fig. 21 illustrates the Froude number distribution obtained from the performed simulations. The evaluated profiles are consistent across the tested scales indicating that the captured dynamic response is identical between the original simulation and the upscaled configurations.

Scaling the geometry of the model leads to increasing the velocity as well as, the depth of the granular flow and therefore, the Fr number maintains the same value in all models. The observed similarity in the constructed models ensures the validity of scaling the experimental observations to reflect the behaviour of the large-scale numerical models.

Scheidl et al. [11] suggest that given a consistent dynamic response across different scales, the soil pressures recorded at the face of a rigid obstacle in a laboratory test can be adjusted by the geometric scaling factor (λ) to replicate realistic conditions. The geometric scaling factor, $\lambda = l^*/l$, is equal to the ratio between the dimensions of the prototype (l^*) and laboratory (l) setups. Accordingly, the soil pressures (p^*) at the face of the obstacle in large scale configurations is evaluated upon the corresponding experimental measurements (p) as demonstrated in Equation (6). In all subsequent analytical derivations, variables denoted with an asterisk (*) correspond to the scaled configurations, while the plain variables represent the values of the original model.

$$p^* = p\lambda \tag{6}$$

The validity of the proposed analytical formulation is tested with the numerical results obtained from the performed simulations. The normal forces measured at the face of the obstacle are normalised by the front area of the element to evaluate the induced soil pressures.

Fig. 22 illustrates the magnitude of soil pressures obtained from both the experimental and the upscaled configurations. The consistent evolution of earth pressures in all models, reveals that the captured response of the soil flows and the impact mechanisms remain identical across the scales. However, it is observed that the duration of the simulated soil flows increases with the scale of the model. Therefore, the analyses' timespan for the large-scale configurations is appropriately extended to

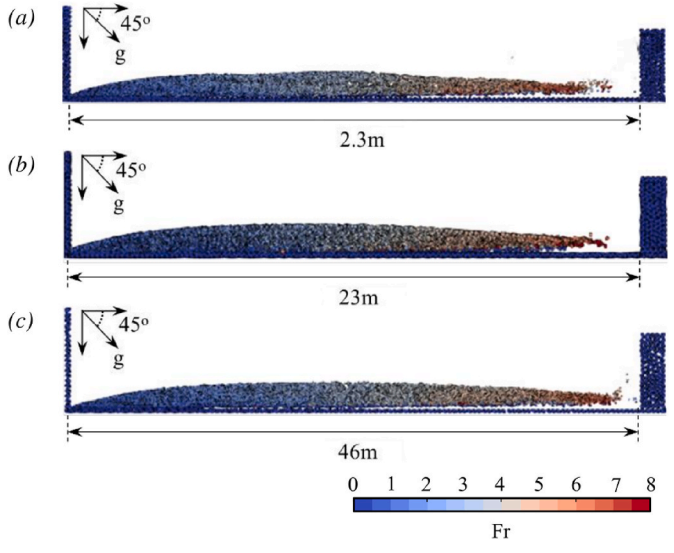

Fig. 21. Froude number distribution from geometrically scaled models by (a) $\lambda = 1$ (original setup) (b) $\lambda = 10$ & (c) $\lambda = 20$ (λ denotes the scale factor).

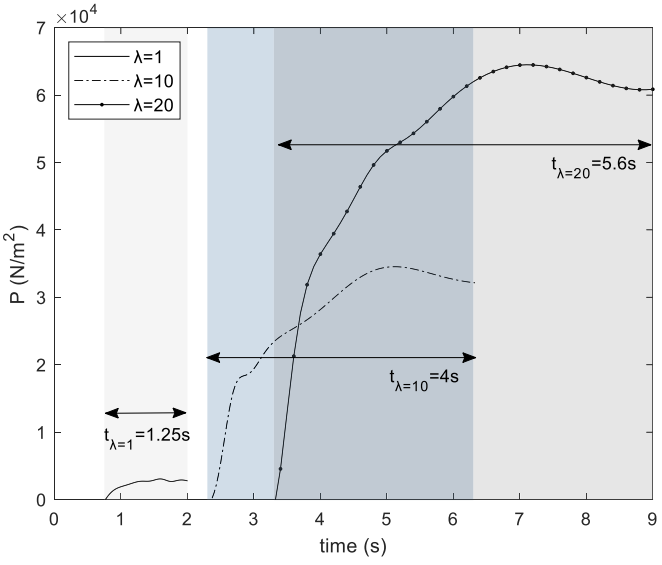

Fig. 22. Soil pressures (P) normal to the obstacle from the scaled simulations by $\lambda = 1, 10, 20$.

achieve a consistent deformed shape for the granular flows with the one predicted through the small-scale simulation within 2s. The time required to achieve the same response in all models is highlighted in Fig. 22 through the marked arrows.

The ratio of the maximum impact pressures derived from the large-scale and the original model reflects the geometric scale ratio and confirms the applicability of Equation (6). The experimental geometry is modified by the factor λ in all the dimensions of the setup, i.e. $b^* = b\lambda$, $l^* = l\lambda$ to replicate prototype conditions. Subsequently, to evaluate the scaling factor for the impact forces the validated formulation is modified as shown in Equation (7). The derived factor for the forces complies with past recommendations from the literature (e.g. [22,42]), provided that the density of the involved materials is constant among the prototype and small-scale setups.

$$p^* = p\lambda \leftrightarrow \frac{F^*}{b^* l^*} = \frac{\lambda F}{bl} \leftrightarrow \frac{F^*}{\lambda^2 bl} = \frac{\lambda F}{bl} \leftrightarrow F^* = \lambda^3 F \tag{7}$$

To further investigate the scaling effect on the response of the granular flow, Fig. 23 presents the soil depth along the flume, as recorded in the performed simulations, normalised by the corresponding scaling factors. The graph accounts for the height of the earth flows prior to the soil impacting the obstacle. The obtained curves demonstrate that the ratio of the measured flow depths from the scaled models to those associated with the original simulation is equal to λ, i.e. $h_f^* = h_f\lambda$. The horizontal axis, denoted as the distance along the flume (x), is normalised with respect to the maximum runout distance of the flow (λL), i.e. $\overline{X} = \frac{x}{\lambda L}$. The values of L are determined as 1.8 m for the experimental simulation, as well as 18 m and 36 m for the scaled models with factors $\lambda = 10$ & 20, respectively.

The velocity of the soil flow increases with the scale of the models, as observed in Fig. 24(a). The graph presents the kinematics of the MPs monitored, indicatively, at a section located 0.4λ upstream of the obstacle. Equation (5) is employed to formulate an analytical relationship, that adjusts the velocity measured in the small-scale model to represent the kinematics observed in prototype conditions. Since the *Fr* distribution of the simulated soil flows remains consistent across the scales, and the flow height increases proportionally with the deployed geometric scaling factor, the velocity of the large-scale flow can be estimated using Equation (8).

$$Fr = Fr^* \leftrightarrow \frac{v}{\sqrt{glcos\alpha}} = \frac{v^*}{\sqrt{g\lambda l\, cos\,\alpha}} \leftrightarrow v^* = \sqrt{\lambda} v \tag{8}$$

To evaluate the effect of scaling on the duration of the soil flow, Equation (8) is modified by expressing the velocity as the rate of displacement.

$$v^* = \sqrt{\lambda} v \leftrightarrow \lambda \frac{dx}{dt^*} = \sqrt{\lambda}\, \frac{dx}{dt} \leftrightarrow dt^* = \sqrt{\lambda} dt \tag{9}$$

To validate the derived scaling factors, the average velocity of the integration points along the depth of the defined sections are normalised by $\sqrt{\lambda}$ and presented in Fig. 24(b) as a function of time. The similarity of the normalised curves indicates the reliability of the estimated factors.

Fig. 25 illustrates the normalised duration of the impact across the

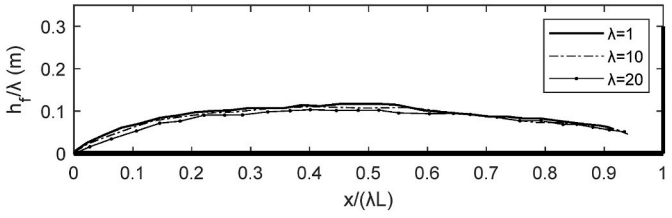

Fig. 23. Flow height prior to the impact normalised by λ for the conducted simulations.

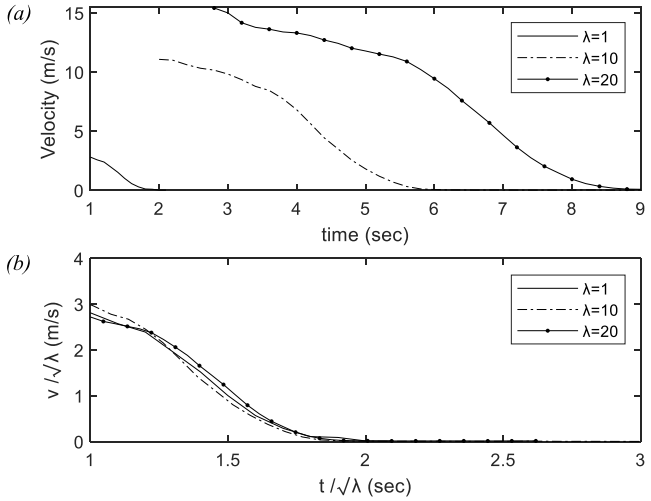

Fig. 24. (a) Average flow velocity upstream of the obstacle, (b) Normalised velocity by $\sqrt{\lambda}$.

tested configurations by $\sqrt{\lambda}$, along with the soil pressures recorded at the face of the obstacle by λ. The curves exhibit a consistent trend, indicating that the captured impact mechanisms and stress evolution are identical.

The numerical results, depicted in Fig. 26, point out that the captured strain profiles are identical across the scales. This observation suggests that the rate of deformation obtained at each analysis step remains constant between the compared configurations, despite modifying the dimensions of the upscaled models. The observed similarity in *Fr* numbers among the different systems emphasizes that the dynamic behaviour of the simulated granular flows is identical. Consequently, it is expected that the same level of deformation will occur in each system.

To comprehend the observed consistency in the magnitudes of acceleration obtained from the conducted analyses, the parameters involved in the equation of motion describing the behaviour of the small-scale and prototype systems are investigated. The assigned soil properties in all models irrespective of their geometry remain constant. Therefore, the mass is solely scaled by λ^3 and λ^2, considering the adjustments performed to the dimensions of the soil box to account for the three- and two-dimensional aspects of the model, respectively. The external gravity loads applied to the system vary with the scale of the

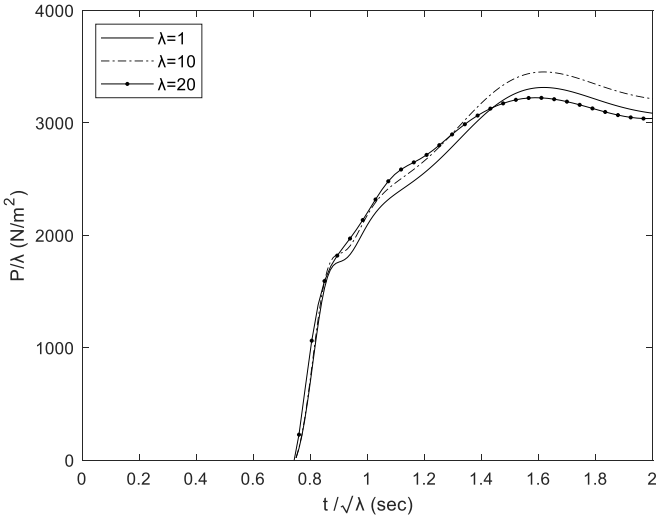

Fig. 25. Normalised soil pressures (P) and duration of the impact by λ and $\sqrt{\lambda}$ respectively.

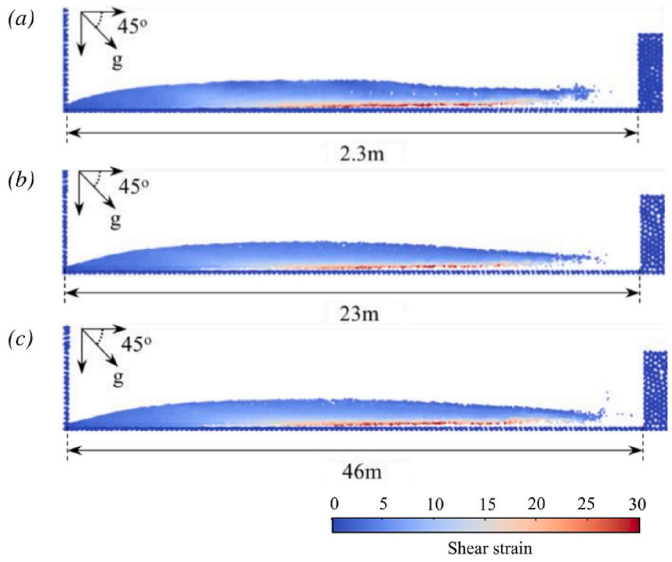

Fig. 26. Shear strain profile across scaled models by (a) $\lambda = 1$, (b) $\lambda = 10$, (c) $\lambda = 20$.

simulation upon the mass of the granular material. In addition, the formulation to evaluate the stiffness of a soil column, provided in Equation (10), indicates that the variable increases linearly by λ in the plane of the model. Hence, if zero damping is applied to the response of the flow, the form of the equation of motion remains consistent across the scales. Consequently, Equation (11) demonstrates that the attained range of acceleration does not vary upon the applied modifications to the geometry of the original model.

$$K^* = \frac{EA^*}{l^*} \leftrightarrow K^* = \frac{E\lambda^2 A}{\lambda l} \leftrightarrow K^* = \lambda K \tag{10}$$

$$F^* = m^* a^* + K^* u^* \leftrightarrow \lambda^2 mg = \lambda^2 m a^* + \lambda K \lambda u \leftrightarrow F = m a^* + Ku \tag{11}$$

The present numerical investigation led to obtaining factors to adjust the results of a small-scale simulation to describe the response of prototype models. The suggested factors, summarised in Table 4, are validated by means of numerical modelling on the condition that *Fr* similarity is maintained across the different scales. Similar parameters to the proposed ones are suggested by Iai et al. [22] to modify the results of a virtual 1g setup to reflect the response of a large-scale system. Besides geometric scaling (μ), Iai et al. [22] also account for parameters that address the influence of scaling on the density (μ_ρ) and the strain (μ_ε) of the systems by incorporating relevant factors. The present study assumes that the density of the granular material is identical in the original model and the enlarged models, therefore, μ_ρ is equal to 1. In addition, the adopted numerical technique considers the macroscopic behaviour of the soil material and does not capture the effect of scaling on the granular mixture, which could potentially affect the strain profile. As a result, the strain consistency across scales results into a μ_ε value of 1, indicating that the scaling principles of Iai et al. [22] align with the factors derived from this study.

Table 4
Scaling factors.

Variable	Symbol	Factor	Iai et al. [22]
Length (m)	l^*, h^*, w^*	λ	μ
Density (kg/m3)	ρ^*	**1**	μ_ρ
Mass (kg)	m^*	λ^3	–
Displacement (m)	x^*	λ	$\mu\mu_\varepsilon$
Pressure (N/m²)	p^*	λ	$\mu\mu_\rho$
Impact Force (N)	F^*	λ^3	$\mu^3\mu_\rho$
Flow Height (m)	$h_f{}^*$	λ	–
Strain	ε^*	**1**	μ_ε
Velocity (m/s)	v^*	$\sqrt{\lambda}$	$\sqrt{\mu\mu_\varepsilon}$
Time (s)	t^*	$\sqrt{\lambda}$	$\sqrt{\mu\mu_\varepsilon}$
Stiffness (N/m)	K^*	λ	$\mu\mu_\rho/\mu_\varepsilon$
Acceleration (m/s)	a^*	**1**	1

Notably, our numerical models demonstrate negligible sensitivity to the performed scaling. Although the velocity increases with upscaling the original simulation, the deformation of the soil mass in the large-scale systems is consistent with the shape of the flow captured through the model of the experiment. The numerical analysis indicates an inability in addressing the increased turbulence associated with the enhanced kinematics of the granular flow with the scale. The present limitation is attributed to the deployed constitutive model which cannot capture potential variability in the viscosity of the flow. Kesseler et al. [15] employed a different geomechanical modelling approach, the Discrete Element Method (DEM), to investigate the efficacy of this technique in addressing the impact of numerical scaling on an experimental flume setup. The authors commented on the inadequacy of DEM to capture scale effects related to soil particle interactions, dust generation, particle fracture mechanisms, and variations in the flow performance due to the increasing Reynolds numbers. Both numerical methods, adopting a different analysis approach, are limited in capturing local flow effects at different scales. The validity of the proposed formulations in this study for scaling numerical models is confirmed. However, additional research is needed to fully comprehend the limitations associated with the suggested formulations derived from scaling laboratory experiments. Likewise, in previous studies, the authors highlight the significance of experimental observations in addressing potential scaling effects [15,20].

5. Conclusions

This study focuses on investigating the impact of dry granular flows on elements inducing partial obstruction to the incoming soil flow, by deploying the Material Point Method (MPM). To ensure the reliability of the numerical response, a 2D model of a flume experiment was initially developed. Subsequently, a sensitivity study was conducted concerning the modelling parameters, revealing that:

- Reducing the mesh size along the face of the structure improves the force measurements due to limiting the recorded oscillations.
- Increasing the number of material points (MPs) leads to a convergent numerical solution. However, subsequent increase in the number of MPs beyond the point of numerical convergence yields minimal impact on the results.

The simulated response of the granular flow was consistent with the experiments, but the deployed material model compromised the predicted magnitude of forces, as it has been also noted in the existing literature. While acknowledging this limitation, the model was extended to the 3D domain. The 3D numerical results aligned with the findings from the 2D models, regardless the dimension of the segments provided across the width of the flume. The preliminary modelling steps validated the ability of MPM to appropriately capture the soil-structure interaction and allowed for further modifying the geometry of the element, to facilitate 50% and 25% obstruction to the incoming flow, while also restricting the material from overflowing. To obtain a detailed representation of the flow response around the obstacle, four elements were provided along the width of the flume. The numerical results demonstrated that:

- Reducing the width of the obstacle leads to gradually increasing the peak normal and shear forces acting on the element. In addition, the post peak degrading branch presents a steeper response with respect to the one captured for wider elements.

- The impact of the incoming flow on the obstacle leads to the immediate formation of a stagnant zone. The efficiency of the sediment in limiting the dynamics of the incoming flow and shielding the obstacle improves proportionally with the width of the element. Therefore, the magnitude of the impact force acting on the obstacle reduces as the blockage ratio becomes larger.

Finally, this study investigated the ability of MPM in adjusting the small-scale numerical observations, into efficiently, representing prototype conditions and concluded that:

- Fr scaling adequately interpreted the original observations into describing the upscaled numerical findings. Relevant scaling principles were validated against existing studies in the literature.
- However, MPM addresses solely the bulk response of the granular flow therefore, the credibility of the derived formulations in scaling the experimental response to characterise the natural problem requires further validation upon comparing laboratory observations against field data.

CRediT authorship contribution statement

M. Kontoe: Writing – original draft, Visualization, Methodology, Formal analysis, Conceptualization. **S. Lopez-Querol:** Writing – review & editing, Supervision, Resources, Methodology, Conceptualization. **T. Rossetto:** Writing – review & editing, Supervision, Resources, Methodology, Conceptualization.

Declaration of competing interest

The authors declare that they have no known competing financial interests or personal relationships that could have appeared to influence the work reported in this paper.

Data availability

No data was used for the research described in the article.

Acknowledgments

This study has received funding from the UCL-GRS scholarship awarded to the first author in 2020.

References

[1] AFP. Colombia mourns 273 dead from avalanche in Mocoa. Caracol News; 2017.
[2] RT Staff Reporters. Brazil: death toll from rains in petrópolis rises to 231. The Rio times. 2022.
[3] Stéfano Salles. Petrópolis perdeu pelo menos R$ 665 milhões no PIB com tragédia, diz Firjan. CNN Brasil; 2022.
[4] Ramesh Bhushal. Why are landslides so deadly in Nepal? The Third Pole 2020 [WWW Document].
[5] Bugnion L, McArdell BW, Bartelt P, Wendeler C. Measurements of hillslope debris flow impact pressure on obstacles. Landslides 2012;9:179–87. https://doi.org/10.1007/s10346-011-0294-4.
[6] Hong Y, Wang JP, Li DQ, Cao ZJ, Ng CWW, Cui P. Statistical and probabilistic analyses of impact pressure and discharge of debris flow from 139 events during 1961 and 2000 at Jiangjia Ravine, China. Eng Geol 2015;187:112–34.
[7] Hu K, Wei F, Li Y. Real-time measurement and preliminary analysis of debris-flow impact force at Jiangjia Ravine, China. Earth Surf Process Landforms 2011;36:1268–78. https://doi.org/10.1002/esp.2155.
[8] Wendeler C. Murgangsruckhalt in wildbachen. grundlage zur planung und berechnung von flexiblen barrieren. Zurich: Swiss Federal Institute of Technology Zurich; 2008.
[9] Cui P, Zeng C, Lei Y. Experimental analysis on the impact force of viscous debris flow. Earth Surf Process Landforms 2015;40:1644–55. https://doi.org/10.1002/esp.3744.
[10] Jiang YJ, Towhata I. Experimental study of dry granular flow and impact behavior against a rigid retaining wall. Rock Mech Rock Eng 2013;46:713–29. https://doi.org/10.1007/s00603-012-0293-3.
[11] Scheidl C, Chiari M, Kaitna R, Müllegger M, Krawtschuk A, Zimmermann T, Proske D. Analysing debris-flow impact models, based on a small scale modelling approach. Surv Geophys 2013. https://doi.org/10.1007/s10712-012-9199-6.
[12] Vagnon F, Segalini A. Debris flow impact estimation on a rigid barrier. Nat Hazards Earth Syst Sci 2016;16:1691–7. https://doi.org/10.5194/nhess-16-1691-2016.
[13] Ceccato F. Study of flow landslide impact forces on protection structures with the Material Point Method. In: Landslides and engineered slopes. Experience, theory and practice. Taylor and Francis Inc; 2016. p. 615–20. https://doi.org/10.1201/b21520-68.
[14] Cuomo S, Di Perna A, Martinelli M. Material point method (Mpm) hydro-mechanical modelling of flows impacting rigid walls. Can Geotech J 2021;58:1730–43. https://doi.org/10.1139/cgj-2020-0344.
[15] Kesseler M, Heller V, Turnbull B. A laboratory-numerical approach for modelling scale effects in dry granular slides. Landslides 2018;15:2145–59. https://doi.org/10.1007/s10346-018-1023-z.
[16] Ng CWW, Song D, Choi CE, Liu LHD, Kwan JSH, Koo RCH, Pun WK. Impact mechanisms of granular and viscous flows on rigid and flexible barriers. Can Geotech J 2017;54:188–206. https://doi.org/10.1139/cgj-2016-0128.
[17] Shen W, Zhao T, Zhao J, Dai F, Zhou GGD. Quantifying the impact of dry debris flow against a rigid barrier by DEM analyses. Eng Geol 2018;241:86–96. https://doi.org/10.1016/j.enggeo.2018.05.011.
[18] Moriguchi S, Borja RI, Yashima A, Sawada K. Estimating the impact force generated by granular flow on a rigid obstruction. Acta Geotech 2009;4:57–71. https://doi.org/10.1007/s11440-009-0084-5.
[19] Zanuttigh B, Lamberti A. Experimental analysis of the impact of dry avalanches on structures and implication for debris flows. J Hydraul Res 2006;44:522–34. https://doi.org/10.1080/00221686.2006.9521703.
[20] Iverson RM. The physics of debris flows. Rev Geophys 1997;35:245–96. https://doi.org/10.1029/97RG00426.
[21] Wendeler C, Volkwein A. Laboratory tests for the optimization of mesh size for flexible debris-flow barriers. Nat Hazards Earth Syst Sci 2015;15:2597–604. https://doi.org/10.5194/nhess-15-2597-2015.
[22] Iai S, Tobita T, Nakahara T. Generalised scaling relations for dynamic centrifuge tests. Geotechnique 2005;55:355–62.
[23] Sulsky D, Chen Z, Schreyer HL. A particle method for history-dependent materials. Comput Methods Appl Mech Eng 1994;118:179–96. https://doi.org/10.1016/0045-7825(94)90112-0.
[24] Soga K, Alonso E, Yerro A, Kumar K, Bandara S. Trends in large-deformation analysis of landslide mass movements with particular emphasis on the material point method. Geotechnique 2016;66:248–73. https://doi.org/10.1680/jgeot.15.LM.005.
[25] Fern J, Rohe A, Soga K, Alonso E. The material point method for geotechnical engineering. CRC Press, Boca Raton : CRC Press, Taylor & Francis Group; 2019. https://doi.org/10.1201/9780429028090 [2019.
[26] Bhandari T, Hamad F, Moormann C, Sharma KG, Westrich B. Numerical modelling of seismic slope failure using MPM. Comput Geotech 2016;75:126–34. https://doi.org/10.1016/j.compgeo.2016.01.017.
[27] He M, Ribeiro e Sousa L, Müller A, Vargas E, Sousa RL, Oliveira CS, Gong W. Numerical and safety considerations about the Daguangbao landslide induced by the 2008 Wenchuan earthquake. J Rock Mech Geotech Eng 2019;11:1019–35. https://doi.org/10.1016/j.jrmge.2019.05.004.
[28] Moormann C, Hamad F. MPM dynamic simulation of a seismically induced sliding mass. In: IOP conference series: earth and environmental science. Institute of Physics Publishing; 2015. https://doi.org/10.1088/1755-1315/26/1/012024.
[29] Alsardi A, Copana J, Yerro A. Modelling earthquake-triggered landslide runout with the material point method. Proc Inst Civ Eng: Geotech Eng 2021;174:563–76. https://doi.org/10.1680/jgeen.20.00235.
[30] Alsardi A, Yerro A. Runout modeling of earthquake-triggered landslides with the material point method. American Society of Civil Engineers (ASCE); 2021. p. 21–31. https://doi.org/10.1061/9780784483428.003.
[31] Nakajima S, Abe K, Shinoda M, Nakamura S, Nakamura H, Chigira K. Dynamic centrifuge model tests and material point method analysis of the impact force of a sliding soil mass caused by earthquake-induced slope failure. Soils Found 2019;59:1813–29. https://doi.org/10.1016/j.sandf.2019.08.004.
[32] Zhou S, Stormont J, Chen Z. Simulation of geomembrane response to settlement in landfills by using the material point method. Int J Numer Anal Methods GeoMech 1999;23:1977–94. https://doi.org/10.1002/(SICI)1096-9853(19991225)23:15<1977::AID-NAG45>3.0.CO;2-3.
[33] Yerro Alba. MPM modelling of landslides in brittle and unsaturated soils. Universitat Politecnica de Catalunya (UPC) 2015. Barcelona.
[34] Al-Kafaji IKJ. Formulation of a dynamic material point method (MPM) for geomechanical problems (Doctor of Philosophy (PhD)). University of Stuttgart; 2013.
[35] Mast CM, Mackenzie-Helnwein P, Arduino P, Miller GR, Shin W. Mitigating kinematic locking in the material point method. J Comput Phys 2012;231:5351–73. https://doi.org/10.1016/j.jcp.2012.04.032.
[36] Detournay C, Dzik E. Nodal mixed discretization for tetrahedral elements. In: 4th international FLAC symposium on numerical modeling in geomechanics; 2006. Madrid.
[37] Bardenhagen SG, Guilkey JE, Roessig KM, Brackbill JU, Witzel WM, Foster JC. An improved contact algorithm for the material point method and application to stress propagation in granular material. Computer modeling in engineering and sciences. 2001. p. 509–22.
[38] Anura3D MPM Research Community. Anura3D MPM software - scientific manual. 2021.

[39] Wang L, Coombs WM, Augarde CE, Cortis M, Brown MJ, Brennan AJ, Knappett JA, Davidson C, Richards D, White DJ, Blake AP. An efficient and locking-free material point method for three-dimensional analysis with simplex elements. Int J Numer Methods Eng 2021;122:3876–99. https://doi.org/10.1002/nme.6685.
[40] Coombs WM, Charlton TJ, Cortis M, Augarde CE. Overcoming volumetric locking in material point methods. Comput Methods Appl Mech Eng 2018;333:1–21. https://doi.org/10.1016/j.cma.2018.01.010.
[41] Ceccato F, Simonini P. Granular flow impact forces on protection structures: MPM numerical simulations with different constitutive models. Procedia Eng 2016;158:164–9. https://doi.org/10.1016/j.proeng.2016.08.423.
[42] Kim D, Nam BH, Youn H. Numerical and experimental investigation on the scaling law of strip model foundation on cohesionless soils. KSCE J Civ Eng 2022. https://doi.org/10.1007/s12205-022-1041-1.